

# Quantum Information Scrambling in a Superconducting Qutrit Processor

M. S. Blok<sup>1\*</sup>, V. V. Ramasesh<sup>1\*</sup>, T. Schuster<sup>2</sup>, K. O’Brien<sup>2</sup>, J.M. Kreikebaum<sup>1</sup>, D. Dahlen<sup>1</sup>, A. Morvan<sup>1</sup>, B. Yoshida<sup>3</sup>, N. Y. Yao<sup>2</sup> and I. Siddiqi<sup>1</sup>

<sup>1</sup> *Lawrence Berkeley National Laboratory & Department of Physics,  
University of California Berkeley, CA 94720, USA.*

<sup>2</sup> *Department of Physics, University of California, Berkeley, California 94720, USA.*

<sup>3</sup> *Perimeter Institute for Theoretical Physics, Waterloo, Ontario, Canada.*

*\* These authors contributed equally to this work.*

(Dated: March 9, 2020)

The theory of quantum information provides a common language which links disciplines ranging from cosmology to condensed-matter physics. For example, the delocalization of quantum information in strongly-interacting many-body systems, known as quantum information *scrambling*, has recently begun to unite our understanding of black hole dynamics [1, 2], transport in exotic non-Fermi liquids [3, 4], and many-body analogs of quantum chaos. To date, verified experimental implementations of scrambling have dealt only with systems comprised of two-level qubits [5]. Higher-dimensional quantum systems, however, may exhibit different scrambling modalities [6] and are predicted to saturate conjectured speed limits on the rate of quantum information scrambling [7]. We take the first steps toward accessing such phenomena, by realizing a quantum processor based on superconducting qutrits (three-level quantum systems). We implement two-qutrit scrambling operations and embed them in a five-qutrit teleportation algorithm to directly measure the associated out-of-time-ordered correlation functions. Measured teleportation fidelities,  $F_{\text{avg}} = 0.568 \pm 0.001$ , confirm the occurrence of scrambling even in the presence of experimental imperfections [8, 9]. Our teleportation algorithm, which connects to recent proposals for studying traversable wormholes in the laboratory [10], demonstrates how quantum information processing technology based on higher-dimensional systems can exploit a larger and more connected state space to achieve the resource efficient encoding of complex quantum circuits.

A promising application for near-term quantum information processors is to shed light on fundamental questions in condensed-matter and high-energy physics [11]. An example of such a question – and one which has received a tremendous amount of recent interest – concerns quantum thermalization, the process by which an isolated quantum system evolves (under time-reversible laws) into an equilibrium state with no apparent memory of its starting conditions. Classically, chaos underlies such thermalizing behavior: though ultimately reversible and volume-preserving, chaotic dynamics distort phase space so drastically that even a tiny perturbation spoils time-reversal [12]. In quantum theory, the notion of chaos maps onto the idea of scrambling: many-body evolution which, though ultimately unitary, scatters initially-localized quantum information across all available degrees of freedom [1, 2, 13]. Efficiently realizing such chaotic evolution on a quantum processor is a crucial step towards harnessing quantum computers to answer the question: to what degree does a given many-body system scramble information?

In particular, a quantum processor can help address this question by directly measuring the scrambling-induced spread of initially localized information via out-of-time-ordered correlation functions (OTOCs) [14–17].

In addition to this question’s relevance to fundamental physics, characterizing the scrambling dynamics of a quantum circuit is also of practical importance for the realization of a scalable quantum computer; in partic-

ular, it could help identify many-body noise channels which would be otherwise invisible to conventional verification and validation techniques such as randomized benchmarking [18].

While the majority of current generation quantum processors are based on qubits, qutrit-based (and more generally qudit-based [19]) systems have long been known to exhibit significant advantages in the context of quantum technology: they have been touted for their small code-sizes in the context of quantum error correction [20], high-fidelity magic state distillation [21], and more robust quantum cryptography protocols [22, 23]. To date, advantages of individual qutrits have been explored experimentally in fundamental tests of quantum mechanics [24] and to aid quantum information protocols [25–27], while entanglement between qutrits has been demonstrated in probabilistic photonic systems [28, 29]. A multi-qutrit platform capable of implementing deterministic high-fidelity gates would be a powerful tool to exploit the full potential of qutrits for quantum information processing.

Meanwhile, in the context of scrambling, many questions of interest naturally concern higher-dimensional quantum systems. Quantum simulations using a qudit-based processor, for instance, could help experimentally verify the conjecture that certain large- $N$  gauge theories exhibit the fastest scrambling allowed by nature [7, 30]. Further increasing the qudit dimension, one can also explore the crossover between scrambling be-

havior in discrete- and continuous-variable systems [6], as well as the simulation of higher-spin models such as the Haldane/AKLIT chain and large-central-charge conformal field theories [31–33].

In this Letter, we leverage the extended Hilbert space of qutrits to a similar end: studying many-body scrambling in perhaps its simplest incarnation, a system of two qutrits. In fact, fully scrambling operations in bipartite systems require at least  $d \geq 3$  states. Along the way to implementing and verifying high-dimensional scrambling behavior, we develop and implement a scalable multi-qutrit experimental platform. This platform features long coherence times; multiplexed readout of individual qutrits; fast, high-fidelity single-qutrit operations; and two types of universal multi-qutrit gates for generating entanglement. In addition to studying scrambling, the realization of this processor thus opens the door more generally to quantum logic utilizing qutrits.

Our qutrit processor features eight transmons [34, 35] connected in a nearest-neighbor geometry (Fig. 1a) of which we use five ( $Q_1 - Q_5$ ). Each transmon encodes a single qutrit and is coupled both to a dedicated microwave control line (for performing gates, Fig. 1b) and its own readout resonator (for state measurement, Fig. 1c). Transmons, quantum nonlinear oscillators, have traditionally been operated as qubits using the two lowest-lying energy states  $|0\rangle$  and  $|1\rangle$ ; while their higher energy states ( $|2\rangle$ ,  $|3\rangle$ , etc.) in principle enable transmons to be operated as qutrits (or even qudits), the experimental implementation of qutrit algorithms is challenging owing to: (1) a lack of two-qutrit entangling gates and (2) increased noise associated with higher transmon eigenstates [36].

Overcoming this added noise is necessary to realize high-fidelity operations. Specifically, in transmon qutrits the state  $|2\rangle$  succumbs more quickly to both dephasing (due to charge noise) and energy relaxation processes (due to bosonic enhancement, see Supplementary Information). Using a combination of improved fabrication techniques, careful microwave engineering, and optimized parameter selection (detailed in the Supplementary Information), we achieve long coherence times despite these added noise processes:  $T_1 = (56.0 \pm 10) \mu\text{s}$  ( $(34.8 \pm 4) \mu\text{s}$ ) and  $T_{2,\text{echo}} = (61.2 \pm 11) \mu\text{s}$  ( $(28 \pm 5) \mu\text{s}$ ) for the  $|1\rangle$  ( $|2\rangle$ ) state, averaged over the 5 qutrits. These coherence times allow us to implement 30 ns single-qutrit gates with randomized benchmarking fidelities [18] on par with state-of-the-art qubit processors:  $f_{01} = 0.9997 \pm 0.0001$  and  $f_{12} = 0.9994 \pm 0.0001$ , for gates within the  $\{|0\rangle, |1\rangle\}$  and  $\{|1\rangle, |2\rangle\}$  subspaces respectively.

Armed with high-fidelity single-qutrit gates, we turn to our two-qutrit scrambling unitary,  $U_s$ . This unitary acts as a permutation on the nine two-qutrit computational basis states:  $U_s|m, n\rangle = |2m + n, m + n\rangle$ . It can be implemented using two controlled-SUM gates applied in sequence (Fig. 2c), where the controlled-SUM

is the higher-dimensional analogue of the CNOT gate:  $U_{\text{CSUM}}|m, n\rangle = |m, n + m\rangle$ .

To execute a controlled-SUM gate on our hardware, we exploit its local equivalence to the controlled-phase gate  $U_{C\phi}$ . This two-qutrit entangling gate imprints the phase  $\omega^{mn}$  on each basis state  $|m, n\rangle$ . For qutrits,  $\omega = e^{2\pi i/3}$ , which calls for imparting the phase  $+2\pi/3$  to the states  $|11\rangle$  and  $|22\rangle$ , and the phase  $-2\pi/3$  to the states  $|12\rangle$  and  $|21\rangle$ . The native interaction between transmons in our system—mediated by linear coupling resonators—is described by a ‘cross-Kerr’ Hamiltonian:  $H_{\text{Kerr}} = \alpha_{11}|11\rangle\langle 11| + \alpha_{12}|12\rangle\langle 12| + \alpha_{21}|21\rangle\langle 21| + \alpha_{22}|22\rangle\langle 22|$ . We can imprint arbitrary phases on each two-qutrit eigenstate by interspersing single-qutrit pulses with evolution under this Hamiltonian for appropriately chosen times (see Supplementary Information). This allows us to directly implement a  $U_{C\phi}$  gate in 990 ns, and, combining with additional single-qutrit gates, a scrambling unitary  $U_s$  in 2.01  $\mu\text{s}$ .

In order to characterize the performance of our scrambling unitary (and the constituent CSUM gate), we perform full quantum process tomography on the operation.

This allows us to quantify the process fidelity and understand its error mechanisms.

We find that the dominant error mechanisms are dephasing and amplitude-damping during the cross-Kerr evolution; the maximum fidelities we observe in the CSUM and scrambling unitaries are 0.889 and 0.875, respectively.

Quantum process tomography also allows us to directly visualize the maximally scrambling nature of  $U_s$ , via its effect on local operators (Fig. 2). In particular,  $U_s$  transforms all single-qutrit Pauli operators into fully two-qutrit operators. For comparison, we also illustrate the quantum process maps—both theoretical and experimental—of a single-qutrit unitary that does not delocalize information (Fig. 2a), as well as the entangling (but not fully scrambling) controlled-SUM gate (Fig. 2b). Only in the case of the maximally scrambling  $U_s$  are all one-body operators delocalized (Fig. 2c).

While process tomography provides an elegant way to “image” our two-qutrit unitary’s scrambling behavior, such an approach is infeasible for verifying scrambling in more general many-body operations as it scales exponentially with system size. To this end, we turn to a teleportation algorithm based on the Hayden-Preskill variant of the black hole information paradox [5, 9, 37]. This algorithm quantifies the scrambling behavior of a unitary via a measurement of averaged OTOCs associated with the unitary [1, 30, 38–40]. In this context, maximal scrambling by  $U_s$  is captured by the fact that OTOCs decay to their minimal allowed value ( $1/9$  for a two-qutrit system) [9]. Crucially, the algorithm is constructed in such a way that faithful teleportation of a quantum state  $|\psi\rangle$  requires quantum information scrambling to occur. The teleportation fidelity can in turn be used to *upper-bound*

the OTOC, even in the face of experimental imperfections.

As shown in Fig. 1e, the verification algorithm requires both the scrambling unitary,  $U_s$ , and its time-reversal,  $U_s^*$ , to be performed in parallel on separate pairs of qutrits. The qutrit pairs undergoing forward- and time-reversed- scrambling start out highly correlated: two qutrits out of the four (one from each pair) begin in a maximally entangled Einstein-Podolsky-Rosen (EPR) state,  $|EPR\rangle = (|00\rangle + |11\rangle + |22\rangle)/\sqrt{3}$ . After maximal scrambling, the probability of finding this pair in the same EPR state decreases to  $1/9$ , the same value as if the pair were in a completely random state, owing to entanglement with the other qutrits coupled by  $U_s$ . Simply observing this decrease, however, is not enough to demonstrate scrambling, as it could also have resulted from deterioration of the EPR pair under ordinary experimental decoherence. Here, teleportation comes to our aid: we place one of the remaining two qutrits ( $Q_1$ , the ‘input’) in an arbitrary (unentangled) single-qutrit state  $|\psi\rangle$ , and the other ( $Q_4$ ) in an EPR pair with a fifth qutrit ( $Q_5$ , the ‘output’). Wondrously, in the absence of experimental error, maximally scrambling dynamics imply that whenever  $Q_2$  and  $Q_3$  are measured in their initial EPR state, the state of  $Q_1$  is teleported to  $Q_5$ . Unlike a low EPR measurement probability, high-fidelity teleportation can only occur from true information scrambling, not as a result of decoherence, making the teleportation fidelity a robust diagnostic of information scrambling.

Experimental error will lead to a decay of the teleportation fidelity from unity; nonetheless, *any* fidelity above the classical limit (0.5 for qutrits) places a non-trivial upper-bound on the averaged OTOCs associated with  $U_s$  [9].

In addition to implementing the scrambling unitary, executing the verification algorithm requires the preparation and measurement of two-qutrit EPR pairs. To enable fast EPR preparation, we realize a microwave-driven entangling gate based on the cross-resonance effect [41, 42]. As illustrated in Fig. 3, when one qutrit (the control) is driven at the frequency of its neighbor (the target), the coupling induces Rabi oscillations in the target, with a Rabi frequency dependent on the state of the control. We harness this interaction to implement a conditional- $\pi$  gate,  $U_{C\pi} = (|0\rangle\langle 0| + |2\rangle\langle 2|) \otimes I + |1\rangle\langle 1| \otimes (|0\rangle\langle 1| + |1\rangle\langle 0| + |2\rangle\langle 2|)$ , in 125 ns. In Fig. 3c, we demonstrate how two applications of the conditional- $\pi$  gate are used to prepare a two-qutrit EPR pair. Using state tomography, we measure EPR fidelities  $F_{EPR} = 0.98 \pm 0.002$ .

The final ingredient in the teleportation algorithm is measurement in the EPR basis. Specifically, we project qutrits 2 and 3 into the state  $|EPR\rangle$  while tomographically reconstructing the state of the output qutrit  $Q_5$  to verify successful teleportation. As our architecture natively allows for only computational-basis measure-

ments, we realize the EPR measurement by performing the EPR creation sequence in reverse, transforming  $|EPR\rangle$  to the computational basis state  $|00\rangle$ . We then measure all five qutrits in the computational basis (inserting state-tomography pulses on  $Q_5$  before the measurement), and keep only the measurements showing  $Q_2$  and  $Q_3$  in  $|00\rangle$ . These measurements herald successful teleportation, which we verify by reconstructing the quantum state of  $Q_5$ , represented by the density matrix  $\rho_{out}$ .

The EPR-generation, EPR-measurement, and scrambling pulse-sequences discussed above work particularly well for single pairs of qutrits in “isolation”, i.e. when neighboring qutrits are left in their ground state.

However, for our five-qutrit scrambling algorithm, these operations must work while the other qutrits undergo non-trivial dynamics of their own.

For example, the algorithm specifically requires two neighboring EPR pairs to be created simultaneously and two scrambling operations to be run in parallel (Fig. 1). Because of the “always-on” cross-Kerr interaction, simply applying the basic sequences described above is not sufficient for this purpose; the cross-Kerr interaction would lead to entangling evolution between *all* adjacent qutrits, not just the intended pairs. To combat this unwanted crosstalk, we develop a novel set of dynamical decoupling sequences optimized for qutrits (see Supplementary Information).

The results of the teleportation algorithm are shown in Fig. 4. We perform teleportation of twelve different single-qutrit quantum states (Fig. 4), chosen as the set of single-qutrit Pauli operator eigenstates, which form a state 2-design [43]. After the algorithm is executed, the teleportation fidelity  $F$  is calculated via  $F = \langle \psi_{in} | \rho_{out} | \psi_{in} \rangle$ , and averaged over all initial states. Without making any assumptions about the nature of the noise affecting our quantum processor, the fidelity allows us to upper bound the OTOC by the quantity  $(4F - 1)^{-2}$  [9].

As a control, we first perform the algorithm with the identity operation in place of  $U_s$ . For the sake of comparison, the identity is implemented with the same complexity as the maximally scrambling unitary; indeed, it is performed with exactly the same microwave pulses and delays, with the only difference in the values of the phases of certain software-defined phase gates. Thus, the experimental errors that affect the scrambling unitary should also affect this implementation of the identity. Since the identity is not a scrambling operation, no teleportation should occur and the final state of  $Q_5$  should be maximally mixed regardless of input state, leading to trivial teleportation fidelities  $1/3$ . This is indeed borne out by the data (Fig. 4b).

In contrast, we teleport with markedly higher fidelities under the maximally scrambling unitary: all but one of the input states are teleported with  $F > 0.5$ , and the av-

erage teleportation fidelity is  $F_{\text{avg}} = 0.568 \pm 0.001$ . This allows us to experimentally upper bound the averaged OTOC at  $0.618 \pm 0.004$ , assuming coherent errors.

In summary, we have demonstrated a five-qutrit quantum processor based on superconducting transmon circuits. Using the verification of scrambling as a proof-of-principle task, we have introduced two flavors of entangling gates and simple dynamical-decoupling protocols to ensure that these gates can be run simultaneously. Our qutrit toolbox also features characterization methods such as state- and process- tomography which provide useful information for benchmarking and debugging large-scale computations and simulations. Interestingly, our experiment can be also interpreted from the perspective of quantum error-correction. In that language, our circuit is equivalent to a three-qutrit quantum error-correcting code, which protects information from the erasure of any one of the three qutrits [44]. This perspective also connects our work to the celebrated AdS/CFT correspondence, since it has been suggested that the map from a bulk quantum state in AdS space to the boundary CFT state can also be interpreted as a quantum error-correcting code.

A number of intriguing future directions are suggested by this work. First, our platform opens the door to exploring the potential advantages of ternary quantum logic, including a more efficient decomposition of the Toffoli gate [45] as well as magic state distillation protocols that outperform conventional qubit-based strategies in terms of both error-threshold and yield [21]. Second, the dynamical decoupling techniques introduced here naturally apply to other spin-1 systems including solid-state defect centers and multi-level atomic, molecular and trapped ion systems [46, 47]. Third, one can imagine enlarging the qudit dimension by further leveraging the intrinsic anharmonicity of transmons [48, 49], enabling the study of many-body phases and entanglement dynamics in higher-spin quantum systems [50]. Finally, building upon the tremendous recent excitement surrounding quantum supremacy protocols using pseudorandom quantum circuit sampling [51], it would be natural to investigate analogous qudit-based protocols, where supremacy can be achieved using a substantially smaller number of elements.

**Acknowledgements** The authors gratefully acknowledge the conversations and insights of James Colless, Emmanuel Flurin, Daniel Harlow, William Livingston, Leigh S. Martin, Brad Mitchell and Brian Swingle. This work was supported by multiple grants awarded by the Department of Energy. From the Office of Advanced Scientific Computing Research: the Advanced Quantum Testbed and the Quantum Algorithm Teams Programs. From the Office of High Energy Physics: the HEP QUANTISED and the COMPHEP pilot “Probing information scrambling via quantum teleportation” (DE-

AC02-05CH11231). T.S. acknowledges support from the National Science Foundation Graduate Research Fellowship Program under Grant No. DGE 1752814.

### Author contributions

NY, BY, MB, VR and IS planned and designed the experiment. KO, VR and JMK designed and fabricated the processor. VR, MB, KO, DD and AM set up the experimental apparatus. MB and VR acquired and analyzed the data with contributions from AM and TS. VR, MB, TS and NY wrote the manuscript with contributions from all authors.

- 
- [1] S. H. Shenker and D. Stanford, “Black holes and the butterfly effect,” *Journal of High Energy Physics*, vol. 2014, Mar 2014.
  - [2] P. Hayden and J. Preskill, “Black holes as mirrors: quantum information in random subsystems,” *Journal of High Energy Physics*, vol. 2007, p. 120, Sep 2007.
  - [3] M. Blake, R. A. Davison, and S. Sachdev, “Thermal diffusivity and chaos in metals without quasiparticles,” *Physical Review D*, vol. 96, Nov 2017.
  - [4] D. Ben-Zion and J. McGreevy, “Strange metal from local quantum chaos,” *Physical Review B*, vol. 97, Apr 2018.
  - [5] K. A. Landsman, C. Figgatt, T. Schuster, N. M. Linke, B. Yoshida, N. Y. Yao, and C. Monroe, “Verified quantum information scrambling,” *Nature*, vol. 567, pp. 61–65, Mar 2019.
  - [6] Q. Zhuang, T. Schuster, B. Yoshida, and N. Y. Yao, “Scrambling and complexity in phase space,” *Physical Review A*, vol. 99, Jun 2019.
  - [7] J. Maldacena, “The large  $n$  limit of superconformal field theories and supergravity,” *International Journal of Theoretical Physics*, vol. 38, no. 4, pp. 1113–1133, 1999.
  - [8] B. Yoshida and A. Kitaev, “Efficient decoding for the hayden-preskill protocol,” *arXiv preprint arXiv:1710.03363*, 2017.
  - [9] B. Yoshida and N. Y. Yao, “Disentangling scrambling and decoherence via quantum teleportation,” *Physical Review X*, vol. 9, Jan 2019.
  - [10] A. R. Brown, H. Gharibyan, S. Leichenauer, H. W. Lin, S. Nezami, G. Salton, L. Susskind, B. Swingle, and M. Walter, “Quantum gravity in the lab: Teleportation by size and traversable wormholes,” 2019.
  - [11] J. Preskill, “Quantum Computing in the NISQ era and beyond,” *Quantum*, vol. 2, p. 79, Aug. 2018.
  - [12] M. Kardar, *Statistical Physics of Particles*. Cambridge University Press, 2007.
  - [13] Y. Sekino and L. Susskind, “Fast scramblers,” *Journal of High Energy Physics*, vol. 2008, p. 065, Oct 2008.
  - [14] M. Gärttner, J. G. Bohnet, A. Safavi-Naini, M. L. Wall, J. J. Bollinger, and A. M. Rey, “Measuring out-of-time-order correlations and multiple quantum spectra in a trapped-ion quantum magnet,” *Nature Physics*, vol. 13, pp. 781–786, May 2017.
  - [15] J. Li, R. Fan, H. Wang, B. Ye, B. Zeng, H. Zhai, X. Peng, and J. Du, “Measuring out-of-time-order correlators on a

- nuclear magnetic resonance quantum simulator,” *Phys. Rev. X*, vol. 7, p. 031011, Jul 2017.
- [16] K. X. Wei, C. Ramanathan, and P. Cappellaro, “Exploring localization in nuclear spin chains,” *Phys. Rev. Lett.*, vol. 120, p. 070501, Feb 2018.
- [17] S. Lepoutre, J. Schachenmayer, L. Gabardos, B. Zhu, B. Naylor, E. Maréchal, O. Gorceix, A. M. Rey, L. Vernac, and B. Laburthe-Tolra, “Out-of-equilibrium quantum magnetism and thermalization in a spin-3 many-body dipolar lattice system,” *Nature Communications*, vol. 10, Apr 2019.
- [18] T. Proctor, K. Rudinger, K. Young, M. Sarovar, and R. Blume-Kohout, “What randomized benchmarking actually measures,” *Physical review letters*, vol. 119, no. 13, p. 130502, 2017.
- [19] M. Luo and X. Wang, “Universal quantum computation with qudits,” *SCIENCE CHINA Physics, Mechanics & Astronomy*, vol. 57, no. 9, pp. 1712–1717, 2014.
- [20] E. T. Campbell, “Enhanced fault-tolerant quantum computing in d-level systems,” *Physical Review Letters*, vol. 113, Dec 2014.
- [21] E. T. Campbell, H. Anwar, and D. E. Browne, “Magic-state distillation in all prime dimensions using quantum reed-muller codes,” *Physical Review X*, vol. 2, no. 4, p. 041021, 2012.
- [22] D. Bruss and C. Macchiavello, “Optimal eavesdropping in cryptography with three-dimensional quantum states,” *Physical review letters*, vol. 88, no. 12, p. 127901, 2002.
- [23] H. Bechmann-Pasquinucci and A. Peres, “Quantum cryptography with 3-state systems,” *Physical Review Letters*, vol. 85, no. 15, p. 3313, 2000.
- [24] R. Lapkiewicz, P. Li, C. Schaeff, N. K. Langford, S. Ramelow, M. Wiesniak, and A. Zeilinger, “Experimental non-classicality of an indivisible quantum system,” *Nature*, vol. 474, June 2011.
- [25] A. Fedorov, L. Steffen, M. Baur, M. P. d. Silva, and A. Wallraff, “Implementation of a Toffoli gate with superconducting circuits,” *Nature*, vol. 481, Jan. 2012.
- [26] P. Kurpiers, P. Magnard, T. Walter, B. Royer, M. Pechal, J. Heinsoo, Y. Salathé, A. Akin, S. Storz, J.-C. Besse, S. Gasparinetti, A. Blais, and A. Wallraff, “Deterministic quantum state transfer and remote entanglement using microwave photons,” *Nature*, vol. 558, June 2018.
- [27] S. Rosenblum, P. Reinhold, M. Mirrahimi, L. Jiang, L. Frunzio, and R. J. Schoelkopf, “Fault-tolerant detection of a quantum error,” *Science*, vol. 361, July 2018.
- [28] Y.-H. Luo, H.-S. Zhong, M. Erhard, X.-L. Wang, L.-C. Peng, M. Krenn, X. Jiang, L. Li, N.-L. Liu, C.-Y. Lu, and et al., “Quantum teleportation in high dimensions,” *Physical Review Letters*, vol. 123, Aug 2019.
- [29] P. Imany, J. A. Jaramillo-Villegas, M. S. Alshaykh, J. M. Lukens, O. D. Odele, A. J. Moore, D. E. Leaird, M. Qi, and A. M. Weiner vol. 5, no. 1, pp. 1–10, 2019.
- [30] J. Maldacena, S. H. Shenker, and D. Stanford, “A bound on chaos,” *Journal of High Energy Physics*, vol. 2016, Aug 2016.
- [31] F. D. M. Haldane, “Nonlinear field theory of large-spin heisenberg antiferromagnets: semiclassically quantized solitons of the one-dimensional easy-axis néel state,” *Physical Review Letters*, vol. 50, no. 15, p. 1153, 1983.
- [32] I. Affleck, T. Kennedy, E. H. Lieb, and H. Tasaki, “Rigorous results on valence-bond ground states in antiferromagnets,” in *Condensed Matter Physics and Exactly Soluble Models*, pp. 249–252, Springer, 2004.
- [33] H. Blöte, J. L. Cardy, and M. Nightingale, “Conformal invariance, the central charge, and universal finite-size amplitudes at criticality,” *Physical review letters*, vol. 56, no. 7, p. 742, 1986.
- [34] J. Koch, T. M. Yu, J. Gambetta, A. A. Houck, D. I. Schuster, J. Majer, A. Blais, M. H. Devoret, S. M. Girvin, and R. J. Schoelkopf, “Charge-insensitive qubit design derived from the cooper pair box,” *Physical Review A*, vol. 76, Oct 2007.
- [35] J. A. Schreier, A. A. Houck, J. Koch, D. I. Schuster, B. R. Johnson, J. M. Chow, J. M. Gambetta, J. Majer, L. Frunzio, M. H. Devoret, and et al., “Suppressing charge noise decoherence in superconducting charge qubits,” *Physical Review B*, vol. 77, May 2008.
- [36] M. J. Peterer, S. J. Bader, X. Jin, F. Yan, A. Kamal, T. J. Gudmundsen, P. J. Leek, T. P. Orlando, W. D. Oliver, and S. Gustavsson, “Coherence and decay of higher energy levels of a superconducting transmon qubit,” *Phys. Rev. Lett.*, vol. 114, p. 010501, Jan 2015.
- [37] P. Hayden and J. Preskill, “Black holes as mirrors: quantum information in random subsystems,” *Journal of High Energy Physics*, vol. 2007, no. 09, p. 120, 2007.
- [38] A. Larkin and Y. N. Ovchinnikov, “Quasiclassical method in the theory of superconductivity,” *Sov Phys JETP*, vol. 28, no. 6, pp. 1200–1205, 1969.
- [39] D. A. Roberts, D. Stanford, and L. Susskind, “Localized shocks,” *Journal of High Energy Physics*, vol. 2015, Mar 2015.
- [40] P. Hosur, X.-L. Qi, D. A. Roberts, and B. Yoshida, “Chaos in quantum channels,” *Journal of High Energy Physics*, vol. 2016, Feb 2016.
- [41] J. M. Chow, A. D. Corcoles, J. M. Gambetta, C. Rigetti, B. R. Johnson, J. A. Smolin, J. R. Rozen, G. A. Keefe, M. B. Rothwell, M. B. Ketchen, and et al., “Simple all-microwave entangling gate for fixed-frequency superconducting qubits,” *Physical Review Letters*, vol. 107, Aug 2011.
- [42] C. Rigetti and M. Devoret, “Fully microwave-tunable universal gates in superconducting qubits with linear couplings and fixed transition frequencies,” *Phys. Rev. B*, vol. 81, p. 134507, Apr 2010.
- [43] D. A. Roberts and B. Yoshida, “Chaos and complexity by design,” *Journal of High Energy Physics*, vol. 2017, Apr 2017.
- [44] R. Cleve, D. Gottesman, and H.-K. Lo, “How to share a quantum secret,” *Physical Review Letters*, vol. 83, no. 3, p. 648, 1999.
- [45] P. Gokhale, J. M. Baker, C. Duckering, N. C. Brown, K. R. Brown, and F. T. Chong, “Asymptotic Improvements to Quantum Circuits via Qutrits,” *Proceedings of the 46th International Symposium on Computer Architecture - ISCA '19*, pp. 554–566, 2019. arXiv: 1905.10481.
- [46] C. Senko, P. Richerme, J. Smith, A. Lee, I. Cohen, A. Retzker, and C. Monroe, “Realization of a quantum integer-spin chain with controllable interactions,” *Physical Review X*, vol. 5, no. 2, p. 021026, 2015.
- [47] S. Choi, N. Y. Yao, and M. D. Lukin, “Dynamical Engineering of Interactions in Qudit Ensembles,” *Physical Review Letters*, vol. 119, p. 183603, Nov. 2017.
- [48] Y. Y. Gao, B. J. Lester, K. S. Chou, L. Frunzio, M. H. Devoret, L. Jiang, S. M. Girvin, and R. J. Schoelkopf, “Entanglement of bosonic modes through an engineered exchange interaction,” *Nature*, vol. 566, pp. 509–512, Feb. 2019.

- [49] R. K. Naik, N. Leung, S. Chakram, P. Groszkowski, Y. Lu, N. Earnest, D. C. McKay, J. Koch, and D. I. Schuster, “Random access quantum information processors using multimode circuit quantum electrodynamics,” *Nature Communications*, vol. 8, pp. 1–7, Dec. 2017.
- [50] S. Pai, M. Pretko, and R. M. Nandkishore, “Localization in fractonic random circuits,” *Physical Review X*, vol. 9, no. 2, p. 021003, 2019.
- [51] F. Arute, K. Arya, R. Babbush, D. Bacon, J. C. Bardin, R. Barends, R. Biswas, S. Boixo, F. G. Brandao, D. A. Buell, *et al.*, “Quantum supremacy using a programmable superconducting processor,” *Nature*, vol. 574, no. 7779, pp. 505–510, 2019.

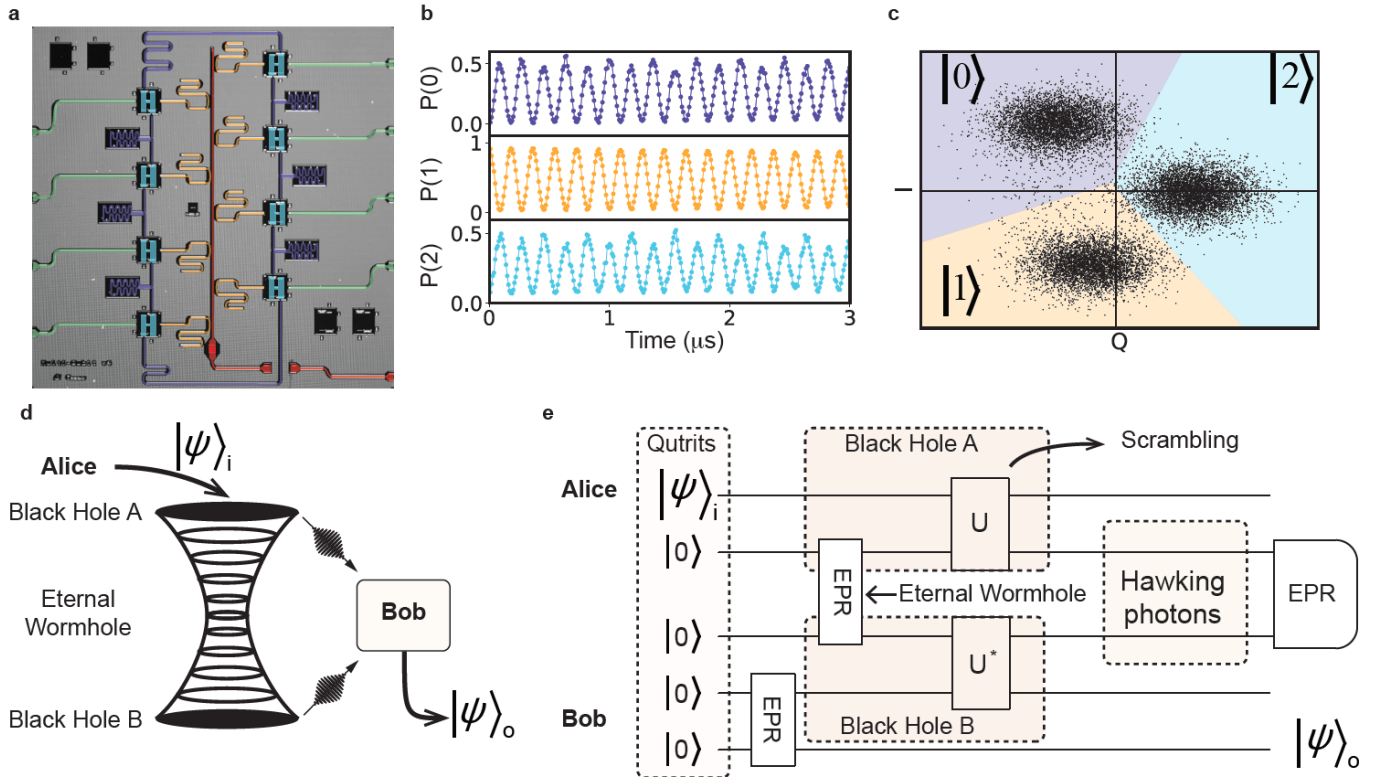


**Figure 1. Superconducting qutrit processor and quantum teleportation circuit** | **a**, Optical micrograph of the five-transmon processor used in this experiment. Transmon circuits (light blue) couple to an integrated Purcell-filter and readout bus (red) via individual linear resonators (gold), enabling multiplexed state measurement. Exchange coupling between nearest-neighbor transmons is mediated by resonators (purple), while microwave drive lines (green) enable coherent driving of individual qubits. **b**, Example coherent Rabi dynamics of a single qutrit induced by microwave driving. Achievable Rabi frequencies are in the range of tens of MHz, three orders of magnitude faster than decoherence timescales. **c**, Example single-shot readout records of an individual qutrit, generally achievable with fidelities above 0.95. This is largely limited by decay during readout. **d-e**, Five-qutrit teleportation algorithm used to test for scrambling behavior of the two-qutrit unitary  $U$ , and its interpretation in the context of black hole physics. Entanglement between two sides of a wormhole is represented by an EPR pair between qutrits 2 and 3, and black hole dynamics by the unitaries  $U$ ,  $U^*$ . A joint EPR measurement between the two sides, corresponding to Hawking radiation in the Hayden-Preskill thought experiment, teleports an arbitrary single-qutrit input state with perfect fidelity if and only if  $U$  is maximally scrambling. In the context of the Hayden-Preskill thought experiment, this protocol is interpreted as one party (Alice) hiding a secret, encoded in a single qutrit, in Black Hole A. The other party (Bob) aims to recover this information through quantum teleportation.

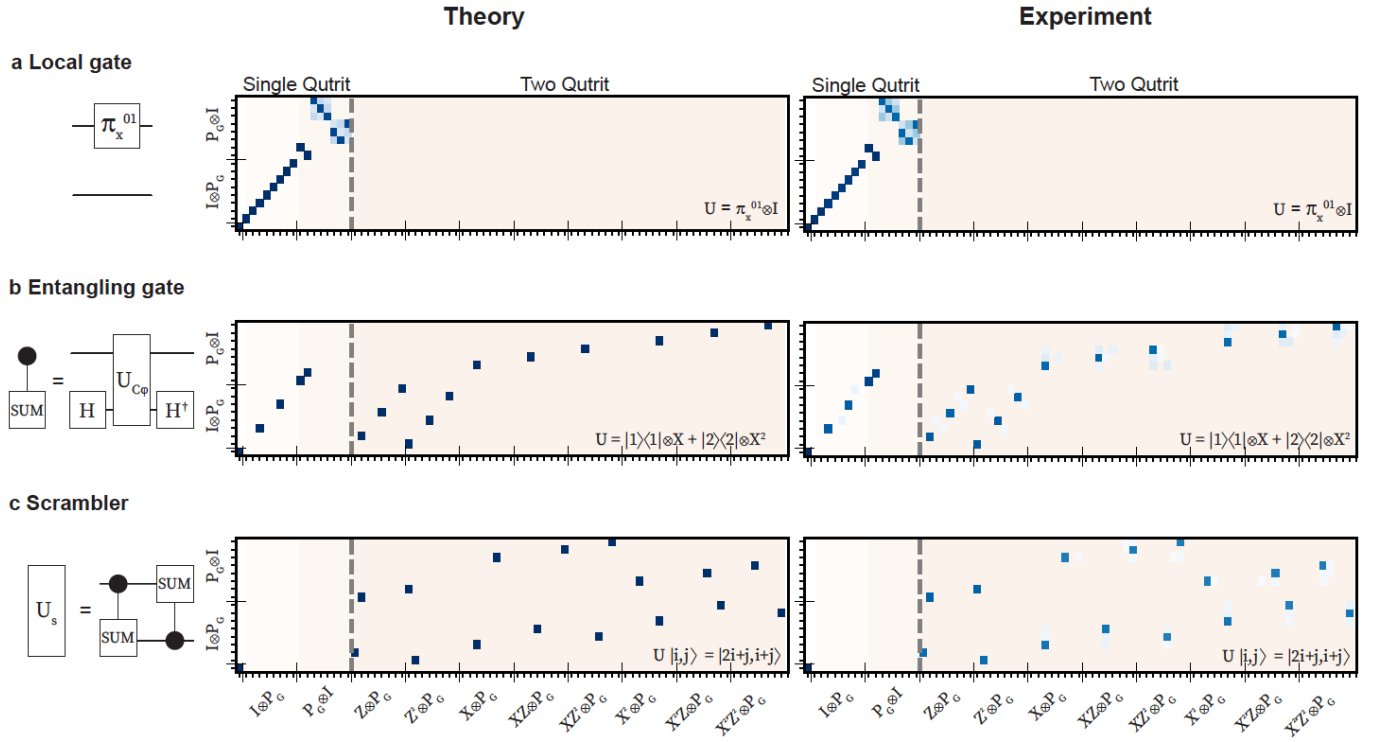


Figure 2. **Implementation and characterization of the two-qutrit scrambling unitary** | **a** Representation of the two-qutrit permutation induced by the maximally scrambling unitary  $U_s$ . **b**, Decomposition of  $U_s$  into two controlled-SUM gates. **c**, Local equivalence between the two-qutrit controlled-SUM gate and a controlled-phase gate  $U_{C\phi}$ , valid for arbitrary system dimension. **d**, Implementation of the controlled-phase gate on the superconducting-qutrit processor from the exchange interaction (see Supplementary Information). **e**, Process tomography, both experimental and ideal, of the scrambling unitary's action on single-qutrit Pauli operators, with tomography of a single-qutrit gate and a non-scrambling entangling gate shown for comparison. This directly verifies the key characteristic of scrambling by  $U_s$ , that it maps all non-identity single-qutrit Pauli operators to two-qutrit operators.



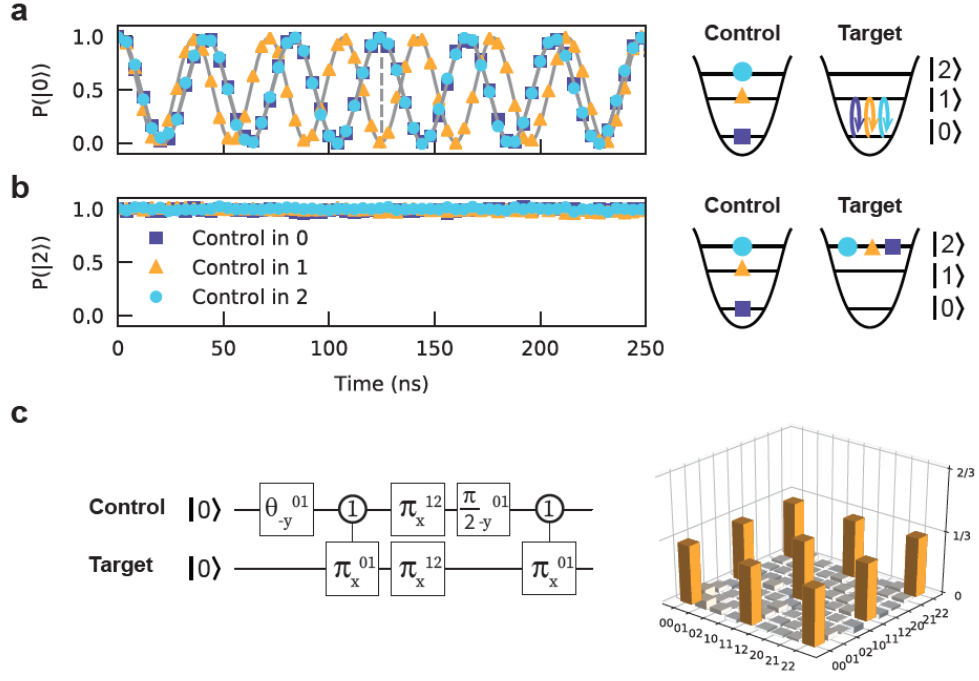
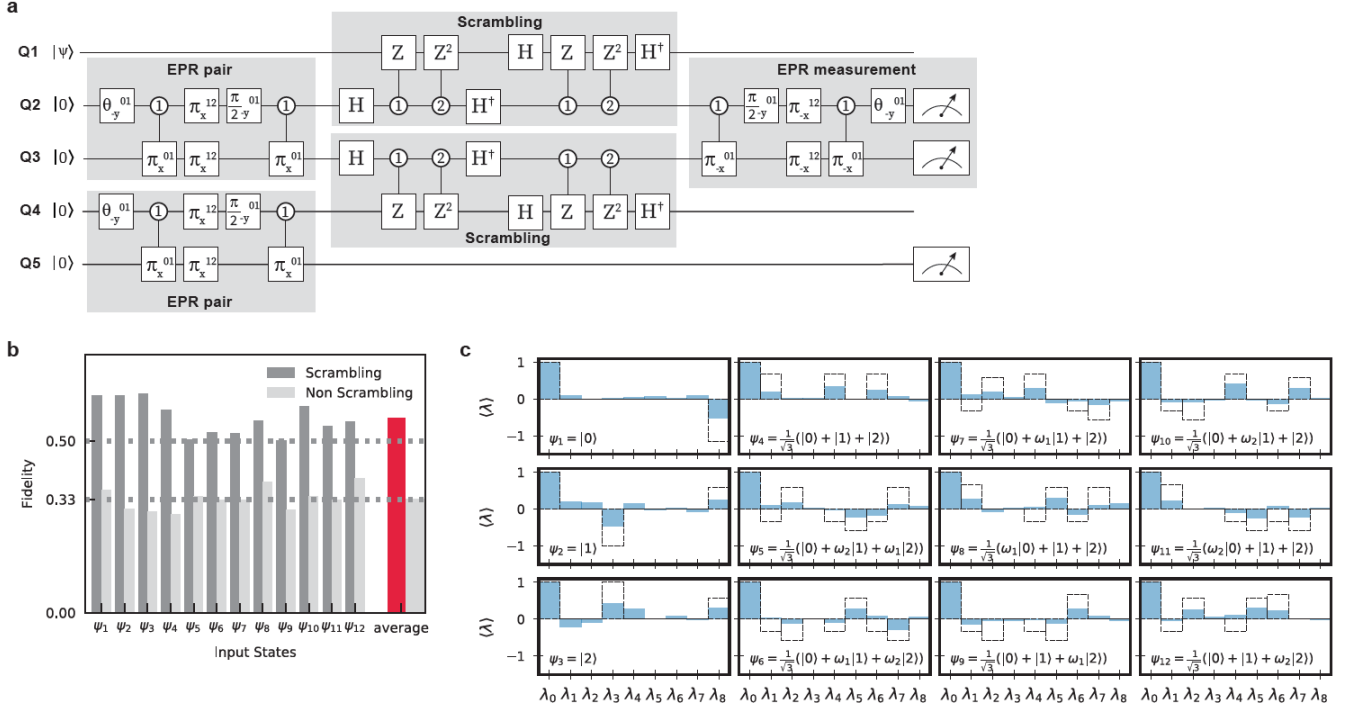


Figure 3. **Two-qutrit EPR pair generation via the cross-resonance interaction** | **a** Nearest-neighbor qutrits coupled by an exchange interaction can be entangled via the cross-resonance effect, where one qutrit (the control) is microwave-driven at the  $|0\rangle \leftrightarrow |1\rangle$  transition frequency of the other (the target). Resulting Rabi oscillations of the target qutrit exhibit a Rabi frequency dependent on the state of the control qutrit. Here, we drive the control with a field whose amplitude is chosen to make the Rabi frequencies corresponding to control states  $|0\rangle$  and  $|2\rangle$  identical, resulting in a unitary operation which, after 125 ns, interchanges states  $|0\rangle$  and  $|1\rangle$  of the target qutrit when the control qutrit is the  $|1\rangle$  state. **b**, When the target qutrit is in the  $|2\rangle$  state, the cross-resonance interaction is off-resonant and does not affect the population. **c**, Sequence used to prepare an EPR pair with two applications of the cross-resonance gate, and the density matrix (reconstructed via state tomography) of the resulting EPR pair, with a state fidelity of  $F_{\text{EPR}} = 0.98 \pm 0.002$ .



## Supplemental Material : Higher Dimensional scrambling

M. S. Blok<sup>1\*</sup>, V. V. Ramasesh<sup>1\*</sup>, T. Schuster<sup>2</sup>, K. O'Brien<sup>2</sup>, J.M. Kreikebaum<sup>1</sup>, D. Dahlen<sup>1</sup>, A. Morvan<sup>1</sup>, B. Yoshida<sup>3</sup>, N. Y. Yao<sup>2</sup> and I. Siddiqi<sup>1</sup>

<sup>1</sup> Lawrence Berkeley National Laboratory & Department of Physics, University of California Berkeley, CA 94720, USA.

<sup>2</sup>Department of Physics, University of California, Berkeley, California 94720, USA.

<sup>3</sup>Perimeter Institute for Theoretical Physics, Waterloo, Ontario, Canada.

\* These authors contributed equally to this work.

### PROCESSOR AND FABRICATION DETAILS

The processor we use features five fixed-frequency (single junction) transmon qutrits on a chip with an eight-transmon ring geometry. The readout and coupling resonators, Purcell filter, transmon capacitors, microwave drive lines and ground plane are composed of niobium, while the transmon junctions are aluminum with an aluminum oxide barrier (Fig 1a main text).

The processor is fabricated on intrinsic  $>8000$  ohm-cm silicon  $\langle 100 \rangle$  wafers. Initial cleaning of the silicon wafer occurs in piranha solution—a mixture of sulfuric acid and hydrogen peroxide—at  $120^\circ\text{C}$  for 10 minutes, followed by 5:1 buffered oxide etch (BOE) for 30 seconds to remove surface contaminants and native oxides. A 200-nm thick film of niobium is then sputtered onto the wafer, with deposition pressures optimized to yield a slightly compressive film. Following this, junctions and all other structures are patterned using 3 rounds of electron-beam lithography. We use MicroChem MMA EL-13 copolymer as a resist, developing it in a 3:1 mixture of IPA:MIBK (isopropyl alcohol and methyl isobutyl ketone) at room temperature for 8 minutes. We then etch the niobium with chlorine chemistry in an inductively coupled reactive ion etcher with about 50 nm overetch into the silicon. After etching, resist is removed with Microposit 1165 at  $80^\circ\text{C}$  for 60 min. The Josephson junction fabrication process begins by stripping native Nb and Si oxides with 30 seconds in BOE. Resist is then spun: we use 500 nm of MMA EL-13 and 150 nm of AllResist AR-P 6200.9, both baked at  $150^\circ\text{C}$  for 60 and 90 seconds, respectively. We write "Manhattan style" junction patterns [1, 2] (proximity-effect-corrected with Beamer by Genisys software) at 100 keV in a Raith EBP 5150 using a 200 pA beam current and 200  $\mu\text{m}$  aperture. After writing, the exposed AR-P is first developed in n-amyl acetate chilled to  $0^\circ\text{C}$ ; after this the AR-P development is halted with 10s immersion in IPA; finally MMA is developed in 3:1 IPA:MIBK for 10 min. We then dry the resulting structure with  $\text{N}_2$  and descum it with an 80W, 200 mbar oxygen plasma etch. This etching step is split into 4 separate substeps, with 90 degree substrate rotations between each substep for improved junction uniformity. Newly-formed oxides at the bottom of the developed structure are then removed with a 15s dip in BOE. The wafer is then loaded into a Plassys MEB550s evaporator and pumped overnight before the junction evaporation steps: first, an Al base electrode is evaporated and the tunnel barrier then formed by thermal oxidation, introducing a 95 % / 5% Ar/O mix into the chamber at 10 mbar for 10 min. A second aluminum electrode is then evaporated to complete the junction and a third evaporation is necessary to climb the second 250 nm capacitor step edge. The junction pattern includes a  $6 \times 8 \mu\text{m}$  Al wire on top of the Nb for electrical contact between the junction and capacitor. After liftoff for 2 hours in acetone at  $67^\circ\text{C}$ , the same resist stack is spun, and  $10 \times 15 \mu\text{m}$  rectangles are opened over the Al/Nb overlap region. The exposed metals are then ion milled and Al is subsequently e-beam evaporated to ensure a low loss galvanic connection between Nb and Al [3]. More details on junction fabrication, including the steps leading to higher uniformity, can be found in [4]. After fabrication, the wafer is diced into  $1 \times 1$  cm dies; cleaned in Microposit 1165 for 12 hours at  $80^\circ\text{C}$ ; sonicated in DI water, acetone, and IPA; descummed in 100 W oxygen plasma for 1 min and then wirebonded into a gold plated copper cryopackage on a 300  $\mu\text{m}$  air gap.

Each transmon is coupled to (i) a linear readout resonator to enable multiplexed dispersive measurement, (ii) two coupling resonators to enable entangling interactions with nearest neighbors, and (iii) a microwave drive line. Readout resonators are loaded so that their effective linewidth  $\kappa_{\text{ext}} \approx 1$  MHz. All readout resonators on the chip are coupled to a common  $\lambda/2$  resonator, a Purcell filter with an external  $Q \approx 10$  [5]. The Purcell filter's passband overlaps with all readout resonator frequencies, allowing fast readout; all qutrit frequencies lie outside the passband, suppressing qutrit relaxation through this channel. Slotline modes of all structures are suppressed using wirebonds; a wirebond also enables the readout bus to overlap a coupling resonator.

## EXPERIMENTAL SETUP

The processor is installed in the 10 mK stage of a BlueFors XLD dilution refrigerator. Room-temperature and cryogenic electronics for performing control and measurement of the qutrit chip are shown in Fig. S1. A Holzworth multi-channel synthesizer generates three local oscillator tones: a qubit control LO at 4.72 GHz, a readout LO at 6.483 GHz, and a pump at 7.618 GHz for the traveling-wave parametric amplifier (TWPAs). Qutrit control pulses are formed by IQ modulating the amplified qubit LO (split six ways) with IF signals from a Tektronix AWG (sample rate 2.5 GS/s) with frequencies between 0.5 and 1.1 GHz. We use both single-channel, hybrid-enabled SSB modulation and high-pass filtering to eliminate the lower sideband of the pulse, with additional band-pass filtering at room-temperature to eliminate noise from the AWG itself. Readout signals are generated using two-channel SSB modulation with IF signals from the same Tektronix AWG. All input signals are further attenuated in the cryostat.

Readout signals are amplified by the TWPA at 10 mK, high-electron mobility transistor amplifiers (HEMT) at 4K, and further amplification at room-temperature before being digitized at 1.25 GSa/s and demodulated in software.

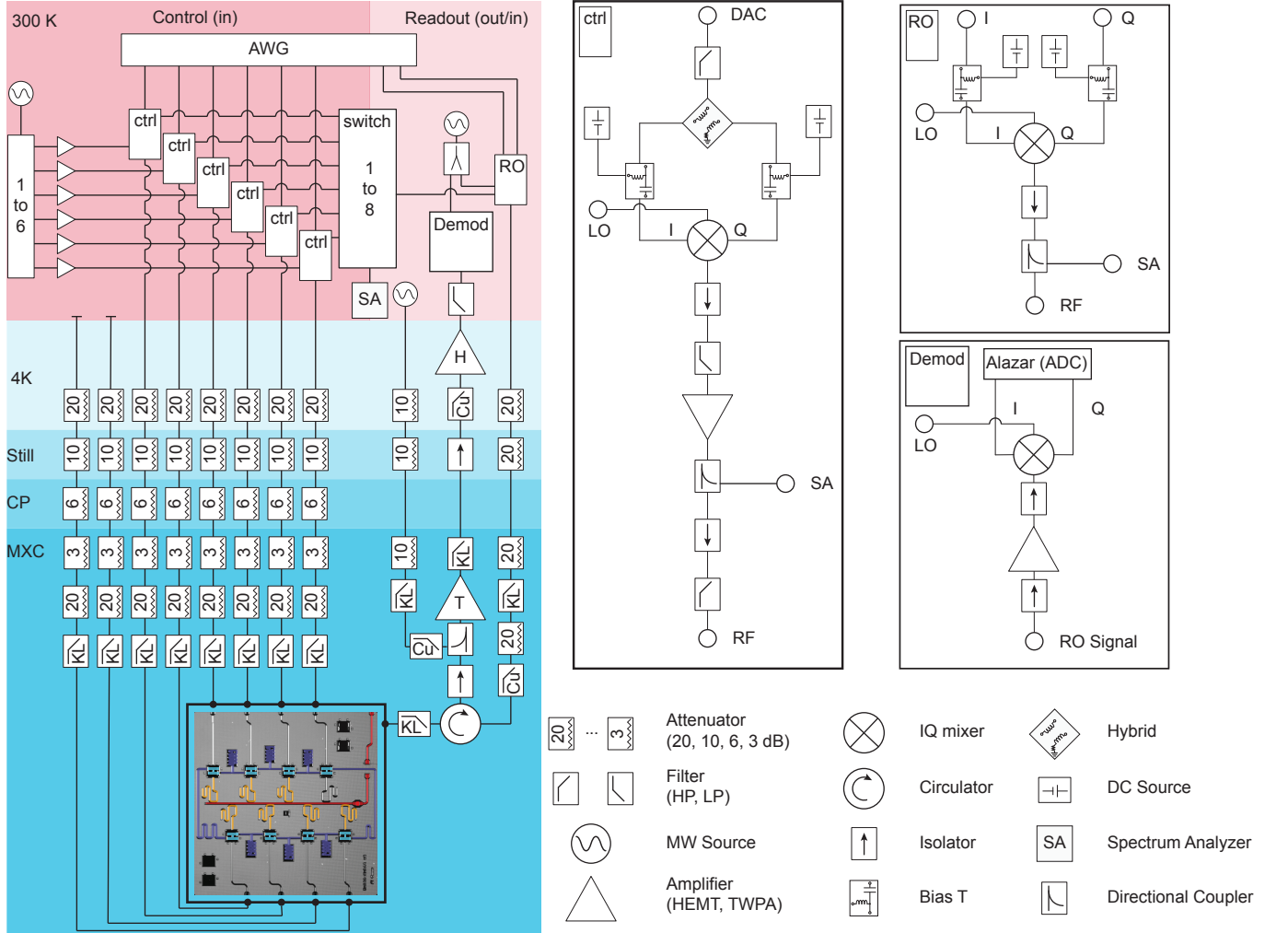


Figure S1. **Experimental setup**

## CHIP CHARACTERIZATION

Transmon parameters are given in Table I. The frequencies are extracted using standard spectroscopy methods. Lifetimes are extracted by fitting decay curves to a single model with five parameters: two energy-relaxation times

	$Q_1$	$Q_2$	$Q_3$	$Q_4$	$Q_5$
Qutrit $ 0\rangle \leftrightarrow  1\rangle$ frequency, $\omega_{01}/2\pi$ (GHz)	5.447	5.634	5.776	5.619	5.431
Qutrit $ 1\rangle \leftrightarrow  2\rangle$ frequency, $\omega_{12}/2\pi$ (GHz)	5.177	5.368	5.512	5.351	5.160
Readout frequency, $\omega_{\text{RO}}/2\pi$ (GHz)	6.384	6.324	6.731	6.673	6.618
Lifetime $T_1^{[1] \rightarrow [0]}$ ( $\mu\text{s}$ )	70	49	43	55	63
Lifetime $T_1^{[2] \rightarrow [1]}$ ( $\mu\text{s}$ )	38	29	39	32	36
Ramsey decay time $T_2^*$ , $ 1\rangle/ 0\rangle$ ( $\mu\text{s}$ )	73	13	41	48	20
Ramsey decay time $T_2^*$ , $ 2\rangle/ 1\rangle$ ( $\mu\text{s}$ )	13	10	16	23	10
Ramsey decay time $T_2^*$ , $ 2\rangle/ 0\rangle$ ( $\mu\text{s}$ )	16	6	15	26	11
Echo time $T_{2\text{Echo}}$ , $ 1\rangle/ 0\rangle$ ( $\mu\text{s}$ )	71	51	46	64	74
Echo time $T_{2\text{Echo}}$ , $ 2\rangle/ 1\rangle$ ( $\mu\text{s}$ )	29	22	22	35	32
Echo time $T_{2\text{Echo}}$ , $ 2\rangle/ 0\rangle$ ( $\mu\text{s}$ )	39	26	34	45	39
Readout fidelity, $ 0\rangle$	0.99	0.99	0.97	0.98	0.99
Readout fidelity, $ 1\rangle$	0.97	0.95	0.94	0.95	0.96
Readout fidelity, $ 2\rangle$	0.95	0.94	0.92	0.95	0.96
Per-Clifford error, $ 1\rangle/ 0\rangle$ subspace	3.6e-4	3.9e-4	5.5e-4	2.7e-4	-
Per-Clifford error, $ 2\rangle/ 1\rangle$ subspace	3.6e-4	6.0e-4	5.0e-4	7.5e-4	-

Table I. Measured properties of the five qutrits

	$Q_1/Q_2$	$Q_2/Q_3$	$Q_3/Q_4$	$Q_4/Q_5$
$\alpha_{11}$	-279	-138	-276	-262
$\alpha_{12}$	160	158	-631	-495
$\alpha_{21}$	-528	-335	243	-528
$\alpha_{22}$	-743	-342	-748	-708

Table II. Cross-Kerr interaction coefficients between nearest-neighbor transmons, given in kilohertz

( $T_1^{1 \rightarrow 0}$  and  $T_1^{2 \rightarrow 1}$ ) and a dephasing time for each basis state. We perform randomized benchmarking to measure pulse errors of single qubit operations in the different subspaces, shown in the table.

We further measure the coefficients of the cross-Kerr (or ‘ZZ’) interaction by performing a Ramsey measurement with neighboring qutrits in the  $|1\rangle$  or  $|2\rangle$  states. The cross-Kerr Hamiltonian between neighboring qutrits is

$$H_{\text{Kerr}}/\hbar = \alpha_{11}|11\rangle\langle 11| + \alpha_{12}|12\rangle\langle 12| + \alpha_{21}|21\rangle\langle 21| + \alpha_{22}|22\rangle\langle 22| \quad (\text{S1})$$

Table II gives the value of these coefficients. Residual cross-Kerr interaction coefficients between non-nearest-neighbor transmons were found to be negligible.

The cross-Kerr interaction is the dispersive limit of an exchange interaction between nearest-neighbor transmons mediated by the coupling resonators, governed by the Hamiltonian

$$H_{\text{int}}/\hbar = g(a^\dagger b + b^\dagger a) \quad (\text{S2})$$

We measure the value of  $g$  on a chip with tunable transmons, but otherwise identical to the one used in the experiment. Spectroscopy of the avoided crossing reveals an interaction amplitude  $g$  of roughly 3 MHz.

### COHERENCE OF THIRD TRANSMON LEVEL

The dominant noise processes affecting transmons tend to worsen for states higher up the transmon ladder. For our qutrit-based processor there are two salient manifestations of this:

- Due to bosonic enhancement, amplitude damping (spontaneous emission) decay from state  $|2\rangle$  to  $|1\rangle$  proceeds roughly twice as fast as the decay from  $|1\rangle$  to  $|0\rangle$ .

- Dephasing due to charge noise, which randomizes the relative phases between the  $|0\rangle$ ,  $|1\rangle$ , and  $|2\rangle$  states, occurs roughly an order of magnitude faster for each state up the transmon ladder: in particular, for the  $|2\rangle$  state relative to the  $|1\rangle$  state.

As stated in the main text, careful fabrication, microwave engineering, and parameter selection were required to obtain high coherence in the transmon qutrit. The fabrication and microwave engineering are detailed in the following Supplemental section, and served to mitigate the  $T_1$  decay. Here we describe the parameter selection – specifically, the choice of the transmon  $E_J/E_C$  ratio – which was chosen to minimize the effect of dephasing.

Transmons are characterized by two parameters: the Josephson energy  $E_J$ , and the capacitive energy  $E_C$  [6]. Increasing the  $E_J/E_C$  ratio exponentially decreases the sensitivity of all transmon eigenstates to charge noise, at the expense of also lowering the transmon’s anharmonicity. Specifically, the charge dispersion  $\epsilon_m$  of the  $m^{\text{th}}$  level is given by

$$\epsilon_m \approx (-1)^m E_C \frac{2^{4m+5}}{m!} \sqrt{\frac{2}{\pi}} \left( \frac{E_J}{2E_C} \right)^{\frac{m}{2} + \frac{3}{4}} e^{-\sqrt{8E_J/E_C}}, \quad (\text{S3})$$

while the relative anharmonicity  $\alpha_r$  is given by

$$\alpha_r \approx -(8E_J/E_C)^{-1/2}. \quad (\text{S4})$$

Typical transmon qubit designs use ratios  $E_J/E_C \approx 50$ . We initially used such a ratio, which resulted in charge dispersion of 102 kHz and <10 kHz of  $|2\rangle$  and  $|1\rangle$  states, respectively. However, with these parameters, charge-parity fluctuations [7] dephase the coherence between the  $|2\rangle$  and  $|1\rangle$  states within 5  $\mu\text{s}$ , making high-fidelity gates impossible to implement. To mitigate this dephasing, we switched to a design with  $E_J/E_C \approx 73$ , which resulted in charge dispersions of 12 kHz and 261 Hz for the  $|2\rangle$  and  $|1\rangle$  states, respectively. This also reduced the anharmonicity from roughly 300 MHz to roughly 250 MHz.

## CROSSTALK

As discussed in the main text, each transmon features a dedicated microwave control line through which we drive single- and two-qutrit gates. However, we find significant (order unity compared to intended coupling) crosstalk between the microwave drive lines for each qutrit. This crosstalk is non-local, not confined to nearest or next-nearest neighbors. When driving Rabi oscillations on a given qutrit, it produces two unwanted effects:

1. All other qutrits will be off-resonantly Rabi driven. Depending on the relative frequencies between the qutrits, this can either manifest as an unwanted change in a qutrit’s state populations (if the frequencies are relatively close) or a Stark shift (if the frequency difference is large compared to the Rabi frequency).
2. Microwave field leaking onto one or more neighboring qutrits will result in an unwanted cross-resonance interaction, making the desired Rabi oscillation frequency vary with the state of the neighboring qutrit(s). This effect was anticipated in [8].

We observed no indications of nonlinearity in the cross-talk at the drive powers we used. That is, for a given drive frequency, the cross-talk can be characterized in terms of a five-by-five complex-valued matrix  $C(\omega)$  relating the field amplitudes  $\vec{o}(\omega)$  seen by each of the five qutrits to the input field amplitudes  $\vec{i}(\omega)$  on each drive line:  $\vec{o}(\omega) = C(\omega)\vec{i}(\omega)$ . We did observe a strong frequency-dependence of the cross-talk matrix.

The linearity of the cross-talk enabled us to compensate for it by inverting the matrix  $C(\omega)$  at each drive frequency, yielding combinations of microwave drive lines which would route the drive field to only a single qutrit. The main challenge in this scheme was the measurement of  $C(\omega)$ . Our strategy was to focus on two drive lines at a time, and find for each line the relative amplitudes and phases which exactly cancelled the field at the location of all of the qutrits on our chip—depending on the relative frequencies, we used either a Stark shift or a Rabi oscillation as a symptom of unwanted microwave field. This measurement was repeated for each of ten drive frequencies of interest (i.e. the  $|0\rangle \leftrightarrow |1\rangle$  and  $|1\rangle \leftrightarrow |2\rangle$  transition frequencies of all five qutrits), each pair of lines, and each qutrit on the chip.

Our crosstalk cancellation method is extremely measurement-intensive and was feasible only because of the relatively few qutrits in this work. On future quantum processors with tens or hundreds of quantum systems, the number of measurements required for our cancellation scheme would be prohibitively expensive. In addition, the strong frequency

dependence of the cross-talk matrix limits the speed at which one can apply single-qudit pulses in this manner: for pulses approximately 10 ns in length, we observed cross-talk which we could not compensate for using our method, likely because of this frequency dependence combined with Fourier broadening of the pulses. Going forward, it is thus important to pinpoint the source of the microwave cross-talk, in order to develop scalable solutions at the hardware level.

### QUTRIT ROTATIONS AND GATE-SET

A convenient set of generators to describe qutrit rotations are the Gell-Mann matrices:

$$\begin{aligned}\lambda_1 \equiv s_x^{01} &= \begin{pmatrix} 0 & 1 & 0 \\ 1 & 0 & 0 \\ 0 & 0 & 0 \end{pmatrix} & \lambda_2 \equiv s_y^{01} &= \begin{pmatrix} 0 & -i & 0 \\ i & 0 & 0 \\ 0 & 0 & 0 \end{pmatrix} & \lambda_3 \equiv s_z^{01} &= \begin{pmatrix} 1 & 0 & 0 \\ 0 & -1 & 0 \\ 0 & 0 & 0 \end{pmatrix} \\ \lambda_4 \equiv s_x^{02} &= \begin{pmatrix} 0 & 0 & 1 \\ 0 & 0 & 0 \\ 1 & 0 & 0 \end{pmatrix} & \lambda_5 \equiv s_y^{02} &= \begin{pmatrix} 0 & 0 & -i \\ 0 & 0 & 0 \\ i & 0 & 0 \end{pmatrix} & \lambda_6 \equiv s_x^{12} &= \begin{pmatrix} 0 & 0 & 0 \\ 0 & 0 & 1 \\ 0 & 1 & 0 \end{pmatrix} \\ \lambda_7 \equiv s_y^{12} &= \begin{pmatrix} 0 & 0 & 0 \\ 0 & 0 & -i \\ 0 & i & 0 \end{pmatrix} & \lambda_8 &= \frac{1}{\sqrt{3}} \begin{pmatrix} 1 & 0 & 0 \\ 0 & 1 & 0 \\ 0 & 0 & -2 \end{pmatrix}\end{aligned}$$

They are the generators of the Lie algebra of the special unitary group SU(3) and can be thought of as the natural extension of Pauli matrices (generators of the Lie algebra of the SU(2) group). For each qutrit (with basis states  $|0\rangle, |1\rangle, |2\rangle$ ), we calibrate a set of microwave pulses that resonantly drive the  $|0\rangle \leftrightarrow |1\rangle$ -transition and a separate set of pulses to address the  $|1\rangle \leftrightarrow |2\rangle$ -transition, providing universal control over the qubit subspaces  $\{|0\rangle, |1\rangle\}$  and  $\{|1\rangle, |2\rangle\}$ . Our microwave control pulses directly perform rotations that correspond to exponentiating Gell-Mann matrices  $s_x^{01}, s_y^{01}, s_z^{01}, s_x^{12}, s_y^{12}$ . The Z-rotation ( $s_z^{01}$ ) is implemented as a virtual Z gate in software by adjusting the phases of subsequent microwave pulses in that subspace [9]. We extend this technique to the 12 subspace to also obtain the following rotation that is not one of the Gell-Mann matrices but that is very useful for single qutrit control since it is a virtual rotation with negligible error:

$$s_z^{12} = \begin{pmatrix} 0 & 0 & 0 \\ 0 & 1 & 0 \\ 0 & 0 & -1 \end{pmatrix} \quad (\text{S5})$$

In principle one could also drive the  $|0\rangle \leftrightarrow |2\rangle$ -transition to directly implement rotations corresponding to  $s_x^{02}, s_y^{02}$ . While it would be worthwhile to add these rotations to the available gate-set to compile circuits with lower depth, these two-photon transitions are more challenging to address as they require high-power. Luckily, all rotations generated by the remaining Gell-Mann matrices can be constructed from our available operations, for example

$$e^{-i\frac{\theta}{2}s_{x/y}^{02}} = e^{-i\frac{\pi}{2}s_x^{12}} \cdot e^{-i\frac{\theta}{2}s_{x/y}^{01}} \cdot e^{i\frac{\pi}{2}s_x^{12}} \quad (\text{S6})$$

where the right most operator is the first to act on the state, so time goes from right to left. Similarly,  $\lambda_8$  can be constructed from  $s_z^{01}$  and  $s_z^{12}$

We write a rotation in one of these subspaces as  $\theta_j^k = e^{-i\frac{\theta}{2}s_j^k}$ , where  $k = \{01, 12\}$  defines the subspace of the rotation,  $j = \{x, y, z\}$  the rotation axis and  $\theta$  the rotation angle. As an example, the two available x-rotations and their corresponding rotation matrices are

$$\theta_x^{01} = \begin{pmatrix} \cos \theta/2 & -i \sin \theta/2 & 0 \\ -i \sin \theta/2 & \cos \theta/2 & 0 \\ 0 & 0 & 1 \end{pmatrix}, \theta_x^{12} = \begin{pmatrix} 1 & 0 & 0 \\ 0 & \cos \theta/2 & -i \sin \theta/2 \\ 0 & -i \sin \theta/2 & \cos \theta/2 \end{pmatrix}, \quad (\text{S7})$$

This notation, combined with some useful qutrit and experiment specific operations, is also adopted in circuit diagrams displayed in the main text and in this document.

Our gate-set consists of all Z-rotations along an arbitrary angle, combined with the Clifford operations operations in the 01 and 12 subspace :

$$\theta_j^k \text{ with } \theta = \{\pi, -\pi, \frac{\pi}{2}, \frac{-\pi}{2}\}, k = \{01, 12\} \text{ and } j = \{x, y, z\}. \quad (\text{S8})$$

Three convenient gates to describe qudit-logic, which can be constructed from our universal gate-set, are the  $X$  and  $Z$  gates

$$X |i\rangle = |i + 1 \bmod d\rangle \quad (\text{S9})$$

$$Z |i\rangle = \omega^i |i\rangle, \quad (\text{S10})$$

where  $\omega = \exp(i2\pi/d)$ .  
and the Hadamard gate

$$H = \frac{1}{\sqrt{d}} \sum_{i,j} \omega^{ij} |i\rangle \langle j| \quad (\text{S11})$$

### CONTROLLED-SUM GATE

In general  $d$ -dimensional qudits, two-qudit controlled-SUM and controlled-phase gates can be defined using the Pauli  $X$  and  $Z$  gates We have:

$$U_{\text{CSUM}}^{01} = \sum_{n=1}^d |n\rangle \langle n| \otimes X^n \text{ and } U_{C\phi} = \sum_{n=1}^d |n\rangle \langle n| \otimes Z^n \quad (\text{S12})$$

Here the superscript 01 indicates that the controlled-SUM is applied with  $Q_0$  as the control qudit and  $Q_1$  as the target; such a label is not necessary for  $U_{C\phi}$ , which is symmetric between the two qudits. The two gates are equivalent up to a single-qudit Hadamard gate  $H$  on the second qudit:

$$(I \otimes H^\dagger) U_{C\phi} (I \otimes H) = U_{\text{CSUM}}^{01}, \quad (\text{S13})$$

where the qudit Hadamard gate is defined to transform the  $Z$  gate into the  $X$  gate under conjugation. Reversing the order of  $H$  and  $H^\dagger$  yields a controlled-MINUS gate, and changing which qubit receives the conjugation interchanges the control and target. The entangling gates  $U_{C\phi}$ ,  $U_{\text{CSUM}}^{01}$ ,  $U_{\text{CSUM}}^{10}$ ,  $U_{\text{CMIN}}^{01}$ , and  $U_{\text{CMIN}}^{10}$  are therefore all equivalent up to local (single-qudit) operations.

In our system, we directly implement the two-qutrit  $U_{C\phi}$  gate by interspersing periods of evolution under the cross-Kerr Hamiltonian (Eq. S1) with single-qutrit gates. Intuitively, evolution under the cross-Kerr Hamiltonian imparts phases to the two-qutrit states  $|11\rangle$ ,  $|12\rangle$ ,  $|21\rangle$ , and  $|22\rangle$ , with values determined by the coefficients  $\alpha_{ij}$ . By interspersing this phase accumulation with single-qutrit pulses exchanging the various states, we can ensure that each state accumulates exactly the phase required for the controlled-phase gate.

We present two methods for implementing the controlled-phase gate in the manner described above. The first uses fewer single-qutrit pulses and is conceptually simpler, but is not dynamically decoupled from the cross-Kerr interaction with neighboring qutrits. The second is dynamically decoupled and is the one used in the teleportation experiment.

**First method:** As depicted in Fig. S2, here we use four periods of cross-Kerr evolution, separated by pulses swapping the  $|1\rangle$  and  $|2\rangle$  states of a single qutrit. Denoting this swap pulse as  $\Pi_q^{12}$ , where  $q$  is the qutrit number, and evolution under the cross-Kerr Hamiltonian for a time  $T$  as  $ZZ_T$ , the total pulse sequence is

$$ZZ_{T_A} \cdot \Pi_0^{12} \cdot ZZ_{T_B} \cdot \Pi_1^{12} \cdot ZZ_{T_C} \cdot \Pi_0^{12} \cdot ZZ_{T_D} \cdot \Pi_1^{12}. \quad (\text{S14})$$

where the times  $T_A$ ,  $T_B$ ,  $T_C$ ,  $T_D$  depend on the cross-Kerr interaction parameters  $\alpha_{ij}$ . For any choice of times, this operation imparts zero phase to the states  $|00\rangle$ ,  $|01\rangle$ ,  $|02\rangle$ ,  $|20\rangle$ ,  $|10\rangle$ , and non-zero relative phases  $\phi_{11}$ ,  $\phi_{12}$ ,  $\phi_{21}$ , and  $\phi_{22}$  to the other basis states. These phases are linear combinations of the delay times  $T_A$ ,  $T_B$ ,  $T_C$ , and  $T_D$ . The transformation from delay times to induced phases is full rank (except for pathological values of the cross-Kerr coefficients), meaning that, given enough total delay time, this method can in principle generate an arbitrary two-qudit phase gate (the states that receive zero phase above can be made to gain arbitrary phase using only single-qutrit



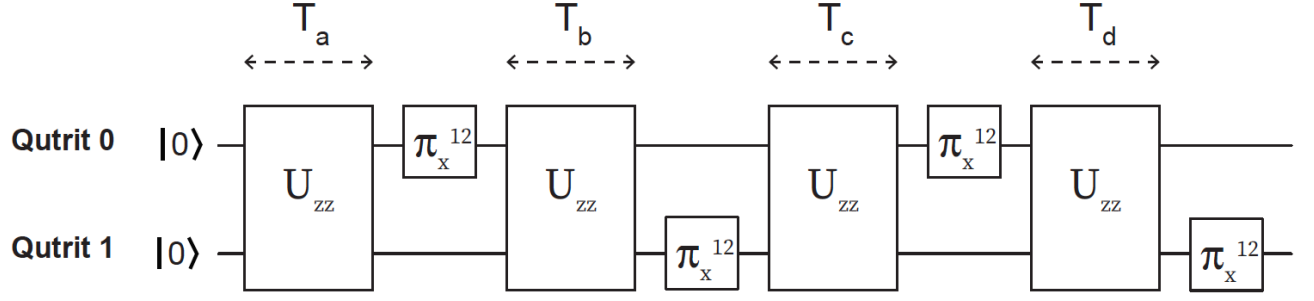


Figure S2. **Four-segment pulse sequence implementing  $U_{C\phi}$**

phase gates). On our particular chip, the coefficients  $\alpha_{ij}$  allow us to implement the controlled-phase in this manner in roughly  $1.5 \mu\text{s}$  for qutrit pairs  $Q_1/Q_2$  and  $Q_3/Q_4$ .

The drawbacks of this method become apparent when one tries to use it in a multi-qutrit algorithm. If the two qutrits undergoing the controlled-phase are coupled to other qutrits via the same cross-Kerr Hamiltonian (as is the case for our chip), the above method will not work when the other qutrits are in superpositions of basis states, in which case entanglement between them and the desired qutrits will be generated. The second method addresses this problem.

**Second method:** As depicted in Fig. S3 a, this method uses six *equal* time periods of cross-Kerr evolution. These are interspersed with single-qutrit pulses swapping the  $|0\rangle/|1\rangle$  and  $|1\rangle/|2\rangle$  subspaces, denoted  $\Pi_q^{12}$  and  $\Pi_q^{01}$ , respectively. The total pulse sequence consists of three repetitions of:

$$[ZZ_T \cdot (\Pi_0^{12} \otimes \Pi_1^{12}) \cdot ZZ_T \cdot (\Pi_0^{01} \otimes \Pi_1^{01})] \quad (\text{S15})$$

For specificity, we have parameterized this pulse sequence with a single delay time,  $T$ ; an appropriately chosen  $T$

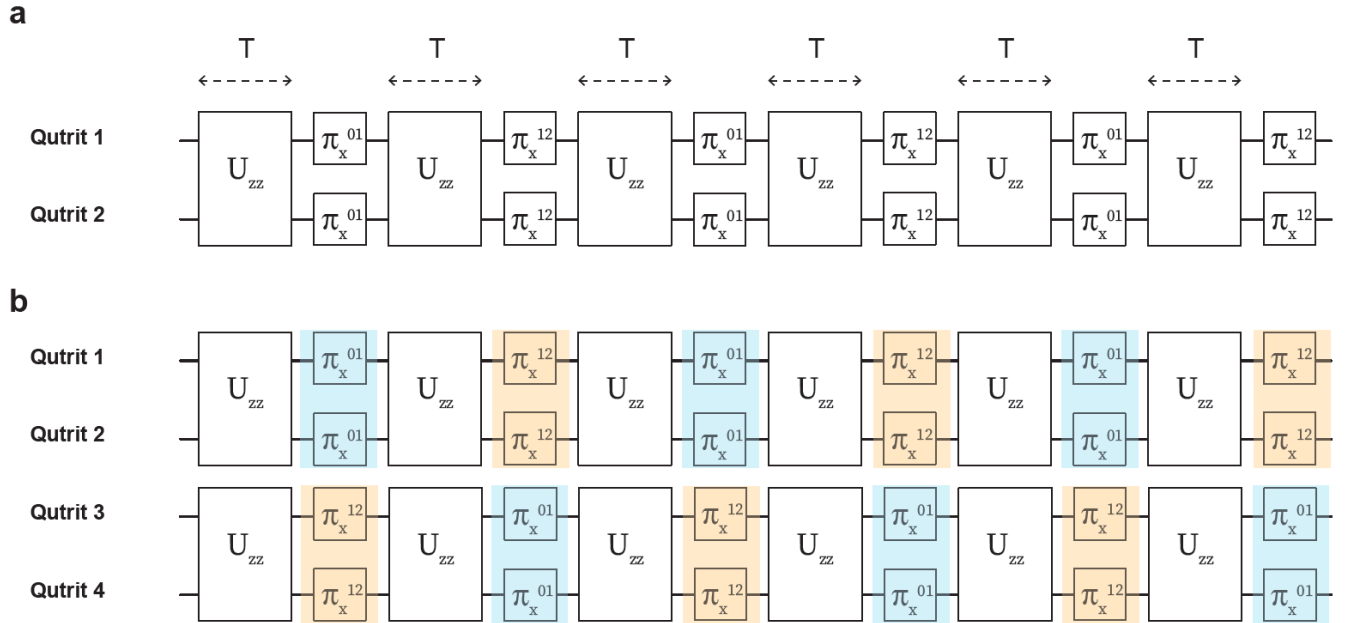


Figure S3. **Six-segment pulse sequence implementing  $U_{C\phi}$ , dynamically-decoupled from static neighbors.**

realizes the controlled-phase gate. The delay time  $T$  is determined by the values of the cross-Kerr coefficients  $\alpha_{ij}$  for each pair  $Q_1/Q_2$  and  $Q_3/Q_4$ , and thus differs between the pairs; however, in practice, we find that a delay of  $192 \text{ ns}$  works well for both.

This pulse sequence constitutes a dynamically-decoupled implementation of the  $U_{C\phi}$  unitary, as its operation is

successful regardless of the states of the neighboring qutrits. The dynamical decoupling arises because the single-qutrit pulses shuffle each qutrit's states  $|0\rangle$ ,  $|1\rangle$ , and  $|2\rangle$  such that an equal amount of time is spent in each state, regardless of the initial state of either qutrit. This shuffling 'averages out' the cross-Kerr interaction with neighboring qutrits, such that no entanglement is generated.

The particular teleportation algorithm we implement requires applying  $U_{C\phi}$  on two pairs of qutrits  $Q_1/Q_2$  and  $Q_3/Q_4$ . We use this dynamically decoupled pulse sequence for both pairs, and apply the gates simultaneously to reduce decoherence associated with a longer total gate time. Naively, the dynamical decoupling effect is weakened by this simultaneity, since the 'neighboring qutrits', with respect to each individual pair, are no longer static. Fortunately, we verify both theoretically and empirically that we can nevertheless decouple the unwanted interaction by reversing the order of the  $\Pi^{12}$  and  $\Pi^{01}$  gates between the two pairs (Fig. S3 b).

### DYNAMICALLY-DECOUPLED EPR PREPARATION

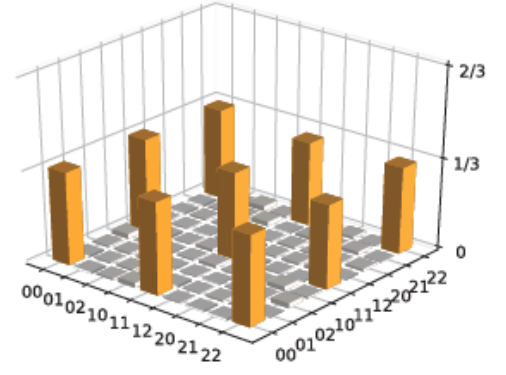
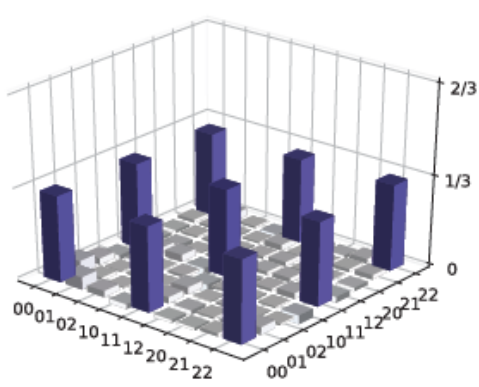
We prepare the two initial EPR pairs of the teleportation algorithm using the controlled- $\pi$  gate as discussed in the main text. The basic sequence is presented in Fig. 3, and serves to prepare an EPR pair on either  $Q_2/Q_3$  or  $Q_4/Q_5$  individually, while all other qutrits are in the ground state  $|0\rangle$ . Simultaneous EPR pair preparation, as required by the algorithm, necessitates a more complicated sequence that incorporates dynamical decoupling. This necessity is demonstrated by Fig. S4(a-b), which compares the result of individual EPR preparation to joint EPR preparation without dynamical decoupling. Joint preparation fidelities are much lower than those of individual preparation. From the measured density matrices, this loss seems to be largely due to a decrease in the off-diagonal elements (i.e. the coherences).

To understand the source of this decrease in coherence, we measured the density matrix of the  $Q_2/Q_3$  EPR pair while projecting the neighboring qutrit,  $Q_4$ , into each of its basis states. Each of the three conditional density matrices we obtained was much purer (i.e. had much higher coherence) than the unconditional density matrix; however, the phases of each coherence differed depending on the state of  $Q_4$ . These measurements suggest that the source of the decoherence was indeed unwanted entanglement between  $Q_3$  and  $Q_4$  arising from the cross-Kerr interaction.

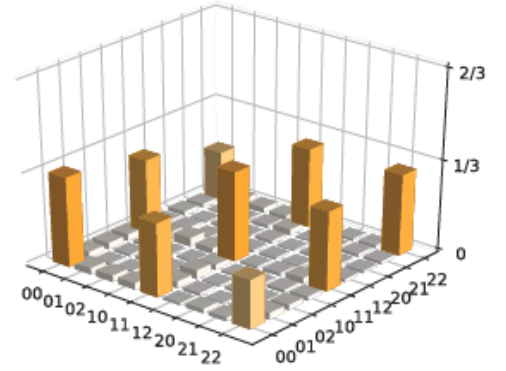
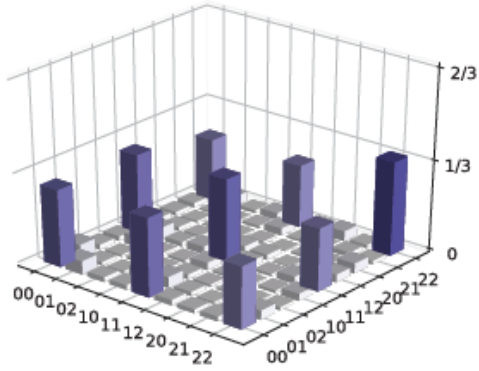
Qutrit State Tomography [10] after each step of the EPR preparation sequence allows us to pinpoint the portions of the sequence that contribute most strongly to the unwanted entanglement. The cross-Kerr interaction affects the  $|2\rangle$  states most strongly, and we find correspondingly that most of the entanglement occurs after the  $|2\rangle$  state of  $Q_3$  gets populated. We take advantage of this by only dynamical decoupling the cross-Kerr interaction after this point. As shown in Fig S5, the initial preparation of Bell states  $(|00\rangle + |11\rangle)/\sqrt{2}$ , which does not involve the state  $|2\rangle$ , is performed without dynamical decoupling to reduce the error associated with additional single-qutrit gates.

The mechanism underlying our decoupling sequence is most easily understood by first considering a simpler problem, of decoupling an unwanted cross-Kerr interaction between two qutrits during an idling period. This can be accomplished by splitting the idling time into three equal time periods, and applying single-qutrit  $X$  gates to one of the qutrits between each of the periods. This shuffling of the populations decouples the entangling interaction into a product of local  $Z$  interactions. Using the same principle, we divide the controlled- $\pi$  operations in the relevant portion of simultaneous EPR preparation into three equal periods of 125 ns, and apply qutrit  $X$  gates on  $Q_4$  in between the periods. This sequence enables simultaneous EPR pair preparation with fidelities  $0.88 \pm 0.002$  and  $0.92 \pm 0.002$  on  $Q_2/Q_3$  and  $Q_4/Q_5$ , respectively.

**a: Individual preparation**



**b: Simultaneous preparation**



**c: Simultaneous preparation with dynamical decoupling**

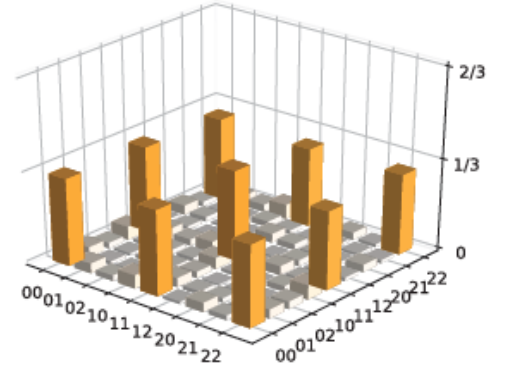
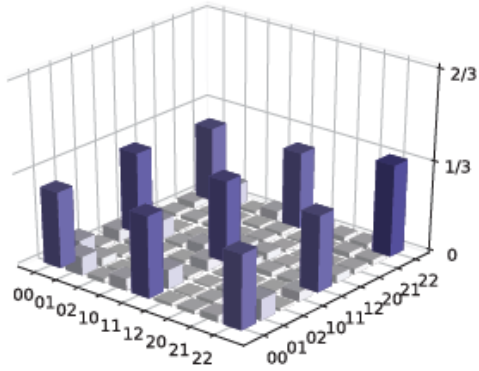


Figure S4. **Dynamically-decoupling the EPR pair preparation** | **a**, Density matrices of the  $Q_2/Q_3$  (left, purple) and  $Q_4/Q_5$  (right, orange) EPR pairs, prepared individually (i.e. with all other qutrits in the ground state). State fidelities for this dataset are  $0.94 \pm 0.002$  and  $0.98 \pm 0.002$  respectively. **b**, Density matrices of the same EPR pairs when prepared simultaneously without any dynamical decoupling. Fidelities are markedly lower in this case,  $0.81 \pm 0.002$  and  $0.82 \pm 0.002$  respectively for the  $Q_2/Q_3$  and  $Q_4/Q_5$  pairs. As discussed in the text, the loss of fidelity is due to unwanted entanglement arising from the cross-Kerr interaction between the two EPR pairs. **c**, EPR pairs prepared simultaneously using dynamical decoupling, with fidelities  $0.88 \pm 0.002$  and  $0.92 \pm 0.002$ , respectively.

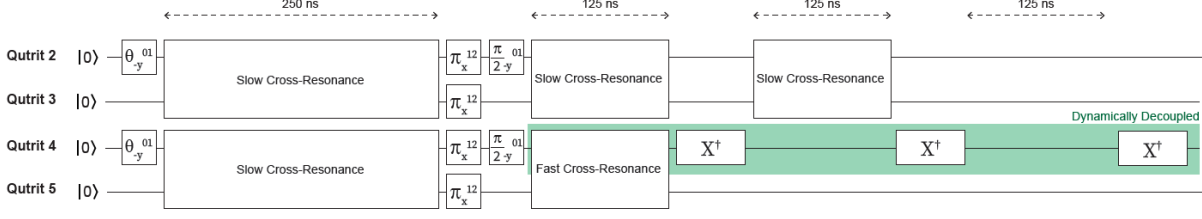


Figure S5. **Dynamically-decoupled gate sequence** The initial step in joint EPR preparation is simultaneous preparation of Bell pairs on both pairs of qutrits. Since the cross-Kerr interaction in the  $|0\rangle/|1\rangle$  subspace is relatively weak compared to the interaction time, little unwanted entanglement occurs during this operation. Following Bell state creation, the remaining evolution is divided into three equal periods of 125 ns, during which the cross-resonance interaction completes the creation of the EPR pairs. In between each period, qutrit  $X$  gates applied on  $Q_4$  serve to dynamically decouple the unwanted cross-Kerr interaction.

- 
- [1] M. V. Costache, G. Bridoux, I. Neumann, and S. O. Valenzuela, "Lateral metallic devices made by a multiangle shadow evaporation technique," *Journal of Vacuum Science & Technology B*, vol. 30, no. 4, p. 04E105, 2012.
  - [2] A. Potts, G. J. Parker, J. J. Baumberg, and P. A. J. de Groot, "Cmos compatible fabrication methods for submicron josephson junction qubits," *IEE Proceedings - Science, Measurement and Technology*, vol. 148, pp. 225–228, Sep. 2001.
  - [3] A. Dunsworth, A. Megrant, C. Quintana, Z. Chen, R. Barends, B. Burkett, B. Foxen, Y. Chen, B. Chiaro, A. Fowler, and et al., "Characterization and reduction of capacitive loss induced by sub-micron josephson junction fabrication in superconducting qubits," *Applied Physics Letters*, vol. 111, p. 022601, Jul 2017.
  - [4] J. M. Kreikebaum, K. P. O'Brien, and I. Siddiqi, "Improving wafer-scale josephson junction resistance variation in superconducting quantum coherent circuits," 2019.
  - [5] E. A. Sete, J. M. Martinis, and A. N. Korotkov, "Quantum theory of a bandpass purcell filter for qubit readout," *Phys. Rev. A*, vol. 92, p. 012325, Jul 2015.
  - [6] J. Koch, T. M. Yu, J. Gambetta, A. A. Houck, D. I. Schuster, J. Majer, A. Blais, M. H. Devoret, S. M. Girvin, and R. J. Schoelkopf, "Charge-insensitive qubit design derived from the cooper pair box," *Physical Review A*, vol. 76, Oct 2007.
  - [7] D. Riste, C. C. Bultink, M. J. Tiggelman, R. N. Schouten, K. W. Lehnert, and L. DiCarlo, "Millisecond charge-parity fluctuations and induced decoherence in a superconducting transmon qubit," *Nature Communications*, vol. 4, May 2013.
  - [8] C. Rigetti and M. Devoret, "Fully microwave-tunable universal gates in superconducting qubits with linear couplings and fixed transition frequencies," *Phys. Rev. B*, vol. 81, p. 134507, Apr 2010.
  - [9] D. C. McKay, C. J. Wood, S. Sheldon, J. M. Chow, and J. M. Gambetta, "Efficient  $z$  gates for quantum computing," *Physical Review A*, vol. 96, Aug 2017.
  - [10] R. Bianchetti, S. Filipp, M. Baur, J. M. Fink, C. Lang, L. Steffen, M. Boissonneault, A. Blais, and A. Wallraff, "Control and tomography of a three level superconducting artificial atom," *Phys. Rev. Lett.*, vol. 105, p. 223601, Nov 2010.